The Astrophysical Journal, 874:56 (16pp), 2019 March 20 https://doi.org/10.3847/1538-4357/ab06f5

Plasma Flows in the Cool Loop Systems

Yamini K. Rao[1], Abhishek K. Srivastava[1], Pradeep Kayshap[2], Klaus Wilhelm[3], and Bhola N. Dwivedi[1]
[1] Department of Physics, Indian Institute of Technology (BHU), Varanasi, India; Yaminikhodia17@gmail.com
[2] Institute of Physics, University of South Bohemia, 370 05, Českè Budjovice, Czech Republic
[3] Max-Planck-Institut für Sonnensytemforschung, Göttingen, Justus-von-Liebig-Weg 3, D-37077, Germany
Received 2018 October 10; revised 2019 February 12; accepted 2019 February 12; published 2019 March 21

Abstract

We study the dynamics of low-lying cool loop systems for three data sets as observed by the *Interface Region Imaging Spectrograph*. Radiances, Doppler shifts, and line widths are investigated in and around observed cool loop systems using various spectral lines formed between the photosphere and transition region (TR). Footpoints of the loop threads are either dominated by blueshifts or redshifts. The cospatial variation of velocity above the blueshifted footpoints of various loop threads shows a transition from very small upflow velocities ranging from $(-1$ to $+1)$ km s^{-1} in the Mg II k line (2796.20 Å; formation temperature: $\log(T/\mathrm{K}) = 4.0$) to the high upflow velocities from $(-10$ to $-20)$ km s^{-1} in Si IV. Thus, the transition of the plasma flows from redshift (downflows) to blueshift (upflows) is observed above the footpoints of these loop systems in the spectral line C II (1334.53 Å; $\log(T/\mathrm{K}) = 4.3$) lying between Mg II k and Si IV (1402.77 Å; $\log(T/\mathrm{K}) = 4.8$). This flow inversion is consistently observed in all three sets of the observational data. The other footpoint of the loop system always remains redshifted, indicating downflowing plasma. The multispectral line analysis in the present paper provides a detailed scenario of the plasma flow's inversions in cool loop systems leading to the mass transport and their formation. The impulsive energy release due to small-scale reconnection above the loop footpoint seems to be the most likely cause for sudden initiation of the plasma flows evident at TR temperatures.

Key words: magnetic fields – magnetohydrodynamics (MHD) – Sun: corona – Sun: magnetic fields – Sun: oscillations

1. Introduction

Physics of the transition region (TR) of the Sun plays an important role in understanding the various dynamical plasma processes. It acts as an interface layer between the chromosphere and the lower corona. The closed magnetic structures are embedded in plasma in different regions of the Sun, e.g., quiet-Sun (QS) and active regions (ARs). The loops are anchored in the solar photosphere while their upper segments may lie either in the chromosphere and TR (low-lying loops), or in the corona. The magnetic loops are classified on the basis of their formation temperatures and emissions. There are hot loops (Dowdy 1993), warm loops (Lenz et al. 1999), and cool loops (Foukal 1976) with temperatures ranging from >2 MK, (1–2) MK, and (0.1–1.0) MK, respectively. This classification also depends on the spectral regime, i.e., cool loops are visible at UV wavelengths, warm loops in extreme ultraviolet (EUV) wavelengths, and hot loops emit ultraviolet (UV), EUV, and X-ray wavelengths. But even cooler loops, possessing temperatures lower than 0.1 MK, also contribute significantly to the EUV emissions (Feldman 1998; Sasso et al. 2012 and references cited therein). There are different scenarios proposed for the heating of such loops, e.g., steady heating, impulsive heating, etc. (Klimchuk 2006).

The loop structures in the solar atmosphere are the manifestations of magnetic structures along which the plasma is confined. In order to understand the heating of loop plasma, thermal diagnostics have to be conducted (Landi 2007). Though the corona sometimes flares in active regions, these loops are mostly considered to remain in a steady state (Rosner et al. 1978). This shows that the heating mechanism has to be steady enough to bring loops in an equilibrium condition. Also, the emission in coronal loops varies significantly, which is found to be more sensitive to density and less to temperature (Benz 2008). Thus, it shows that the diagnostics of flows in coronal loops is not that simple because brightness variations can even be produced by thermal fronts and waves (Reale 2014). Doppler shift measurements for different spectral lines along the line-of-sight direction thus provide some evidence of plasma motions. This supports mainly two types of bulk mass motions: siphon flow often observed in the cool loops due to pressure difference at different footpoints or loop filling and draining, due to momentary heating and cooling, respectively. Significant downflows are driven by cooling for which two mechanisms have been proposed, namely, cool downfalling blobs of plasma or slow magnetoacoustic waves (Bradshaw & Cargill 2005; Cargill & Bradshaw 2013).

Recently, Huang et al. (2015) have provided observational evidence of cool TR loops using Si IV (1402.77 Å) observations of the *Interface Region Imaging Spectrograph* (*IRIS*). However, very few studies have been conducted on cool loops due to instrumental limitations. Earlier, cool loops have been observed using spectral data from other instruments like the Solar Ultraviolet Measurements of Emitted Radiation (SUMER) spectrograph on the *Solar and Heliospheric Observatory* and the EUV Imaging Spectrometer (EIS) on *Hinode*. Doyle et al. (2006) have reported a redshift of ≈20 km s^{-1} in the N V (1238.82 Å) line at the footpoints of cool loops using SUMER observations. Chae et al. (2000) have presented the rotational motions along the axes of the loops having velocities of ≈50 km s^{-1} using H I Lyβ (1025 Å), O VI (1032 Å, 1038 Å), and C II (1037 Å) lines from SUMER in an AR. The inversion of flows from redshift to blueshift has been observed in different regions of the Sun (Brekke et al. 1997; Warren et al. 1997; Chae et al. 1998; Peter & Judge 1999; Teriaca et al. 1999; Dadashi et al. 2011; Kayshap et al. 2015, and references cited therein). However, flows in such cool loop

systems at the chromosphere/TR interface have not been investigated in a detailed manner.

The study of cool loops that are generally invisible at coronal temperatures, and their plasma dynamics, are important candidates to understand correctly the energy and mass transport processes in the solar atmosphere. The heights at which such flows start to propagate upward have not yet been properly understood. In order to understand the formations of cool loops, their energetics and mass supply, as well as the estimation of the flow and structure in such loops are required. Inference of plasma flows in cool loop systems is essential to estimating flows above their footpoints at different heights using different spectral lines with different formation temperatures.

For our investigation in this work, we analyze similar regions using three different data sets comprised of cool loop systems using the spectral lines Mg II k (2796.20 Å) and Ni I (2799.47 Å) in the near-ultraviolet (NUV) domain as well as in far-ultraviolet (FUV) lines C II (1334.53 Å) and Si IV (1402.77 Å) observed by *IRIS* (De Pontieu et al. 2014). We study the Doppler velocity pattern above the footpoints of the cool loop systems as evident in three different spectral observational data sets. The cospatial variation of Doppler velocities above the footpoints of the cool loop systems provides the information about regions where these plasma flows have been triggered. The other characteristic parameters such as radiance and FWHM have also been estimated to provide more insight into the response of the plasma flows in the cool loop systems. Consistency of the results is described in three different epochs of the spectral observations of cool loop systems in different parts of the Sun on different dates. In Section 2, we describe the observational data and their analyses presenting details of all three data sets that have been used. Section 3 describes the results and our interpretation of them, which has been classified into three different subsections of three different data sets. In each subsection, the identification of loops in various spectral lines along with the magnetic polarities at their footpoints—measured with the Helioseismic and Magnetic Imager (HMI) on the *Solar Dynamics Observatory* (*SDO*)—have been discussed. The corresponding parametric maps are shown. The variation of Doppler velocity at the footpoints of the cool loop systems with different spectral lines has also been examined. In the last section, a discussion and our conclusion have been presented.

2. Observational Data and Their Analyses

Spectra from *IRIS* provide data in the FUV band (1331.7–1358.4 Å and 1389.0–1407.0 Å) and in the NUV (2782.7–2835.1 Å) domain with a large number of spectral lines covering the photosphere, chromosphere, TR, and inner corona. Level 2 data are used for this study, which are calibrated for the dark current removal, flat-fielding. We have utilized Si IV (1402.77 Å), Mg II k (2796.20 Å), C II (1334.53 Å), and Ni I (2799.47 Å) spectral lines. We study the cool loop system for three different data sets using these spectral lines. All the data sets used for our analysis have been chosen in such a way that the loop systems should have low connectivity with magneto-plasma threads visible in SJI 1400 Å. The loop systems connected with the outer periphery of an active region or its surroundings should not contain any flare disruption. Also, the loop systems should not contain any jet activity or disruption of field lines during the whole scan of the raster, maintaining the quiet nature of the loops.

Data set 1: The data set used for our study was observed by *IRIS* during the time period from 22:38:08 to 23:11:59 UTC on 2013 December 27 targeting AR 11934. *IRIS* observed raster of 141″ in the *x*-direction and 174″ in the *y*-direction centered at (X_{cen}, Y_{cen}) = (341″, −267″). The raster scan has a temporal cadence of 5.1 s. The whole scan of the raster has 400 pixels in the *x*-direction with the pixel size 0.″35 and 1096 pixels in the *y*-direction with the pixel size 0.″16. The region of interest ranges from 321″ to 399″ in the *x*-direction and −309″ to −245″ in *y*-direction (left column (panels (A), (B), (C), and (D)); Figure 1).

Data set 2: The data set used for our study was observed by *IRIS* during the time period from 02:02:48 to 02:53:46 UTC on 2015 December 10th targeting AR 12465. *IRIS* observed raster of 112″ in the *x*-direction and 119″ in the *y*-direction centered at (X_{cen}, Y_{cen}) = (−615″, −91″). The raster scan has a temporal cadence of 9.6 s. The whole scan of the raster has 400 pixels in the *x*-direction with the pixel size 0.″35 and 1096 pixels in the *y*-direction with the pixel size 0.″16. The region of interest ranges from −609″ to −559″ in the *x*-direction and −79″ to −39″ in the *y*-direction (middle column (panels (E), (F), (G), and (H)); Figure 1). Data set 3: The data set used for our study was observed by *IRIS* during the time period from 19:59:44 to 21:00:57 UTC on 2017 March 29th targeting AR 12645. *IRIS* observed ranges of 141″ in the *x*-direction and 175″ in the *y*-direction centered at (X_{cen}, Y_{cen}) = (−517″, −69″). The raster scan has a temporal cadence of 9.2 s. The whole scan of the raster has 274.50 pixels in the *x*-direction with the pixel size 0.″35 and 200 pixels in the *y*-direction with the pixel size 0.″35. The region of interest ranges from −529″ to −479″ in the *x*-direction and −139″ to −91″ in the *y*-direction (right column (panels (I), (J), (K), and (L)); Figure 1).

We analyze the spectroscopic observations of various lines formed over a broad range of temperatures. We have applied the iris inbuilt routine (i.e., iris_orbitvarr_corr_l2.pro) to remove the orbital variations before applying the fitting procedure. The estimation of rest wavelengths is very crucial for the estimation of Doppler velocities. We estimated the observed wavelengths of neutral lines in the very quiet area (Ni I 2799.474 Å and S I 1401.50 Å). Using the shift of the neutral lines, we have estimated the rest wavelengths of Ni I 2799.474 Å, Mg II k 2796.35, and Si IV 1402.77 Å. We estimate the observed wavelength of C II 1334.532 Å in very quiet conditions, which is used as the rest wavelength of this line. The estimated rest wavelengths of these spectral lines in each data set are tabulated in Table 1. To derive the basic parameters of the line profiles, we use Gaussian fitting to lines of Ni I; formation temperature: $\log(T/\mathrm{K}) = 4.2$ Stucki et al. (2000), Mg II k (2796.20 Å; $\log(T/\mathrm{K}) = 4.0$), C II (1334.53 Å; $\log(T/\mathrm{K}) = 4.3$), and Si IV (1402.77 Å; $\log(T/\mathrm{K}) = 4.8$) (see example fits in Figure 2). The temperature coverage for different lines is indicated as provided by De Pontieu et al. (2014).

We have performed single Gaussian fitting to the Si IV line, inverse Gaussian fitting to the Ni I lines, and single or double Gaussian fitting, depending on the nature of observed profiles, to Mg II k and C II lines. Since Mg II k lines are optically thick, they provide double Gaussian profiles at most of the locations except for sunspots (Morrill et al. 2001; Leenaarts et al. 2013;

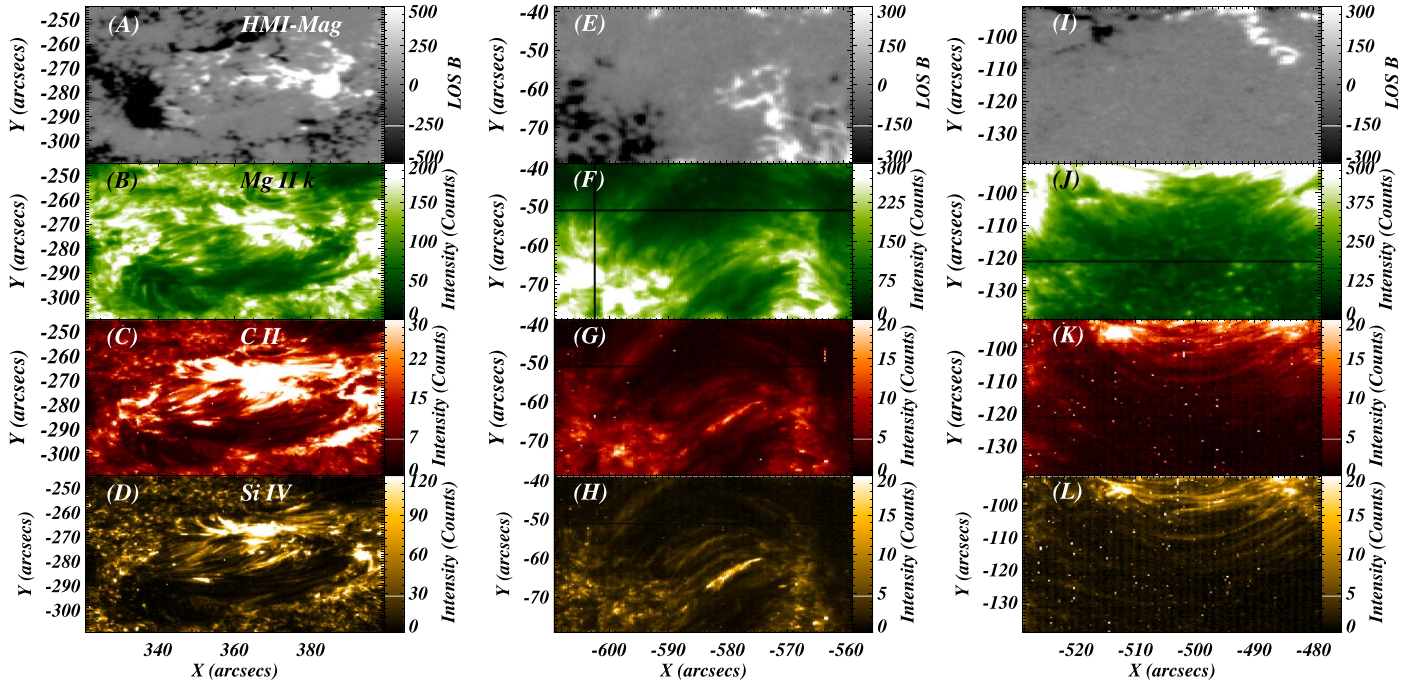

Figure 1. Region of interest displaying the cool loop system in different spectral lines: Mg II k (2796.20 Å), C II (1334.53 Å), and Si IV (1402.77 Å) along with the underlying magnetic polarities indicated by the HMI LOS magnetogram are shown for three different data sets. The left column corresponds to Data set 1 observed on 2013 December 27 targeting AR 11934. The middle column indicates Data set 2 observed on 2015 December 10th targeting AR 12465. The right column shows Data set 3 observed on 2017 March 29 targeting AR 12645.

Table 1
Calibrated Wavelengths for Different Spectral Lines for Different Data Sets

	Ni I (Å)	Mg II k3 (Å)	C II (Å)	Si IV (Å)
Data set 1	2799.4745	2796.3512	1334.5391	1402.7770
Data set 2	2799.4731	2796.3498	1334.5374	1402.7940
Data set 3	2799.4777	2796.3544	1334.5368	1402.8001

Rathore et al. 2015). The details of fitting the optically thick lines are provided in the Appendix.

3. Observational Results and Their Interpretation

3.1. Data Set 1

Identification of the cool loop system. The dynamic loop structures, which are typically visible at low temperatures of the chromosphere and TR, correspond to the cool loops. These cool loop systems are present in all three data sets. The left column of Figure 1 (i.e., panels (A), (B), (C), and (D)) shows the mosaic of intensity images of different spectral lines taken from the *IRIS* raster data along with the LOS magnetogram taken from HMI/*SDO* to show the cool loop system and its footpoint magnetic polarities. To create these intensity images, we have taken the averaged emission within the certain wavelengths around the central wavelengths of these lines, e.g., Mg II (2795.0–2797.2) Å, C II (1334.0–1335.0) Å, and Si IV (1402.0–1404) Å. This system has been taken into consideration as Data set 1. The LOS magnetogram (Figure 1; panel A) shows the presence of opposite magnetic polarities in which the footpoints of the cool loop system lie. This is a multithreaded and dynamic loop system as observed by *IRIS*. In the present study, we use multiple spectral lines covering a wide temperature range to understand the Doppler flow's pattern and its variation in the observed cool loop system. The Mg II k line shows doubly peaked profiles and exhibits emission reversal for all the regions except in the sunspots (Morrill et al. 2001). The Mg II k (panel B; Figure 1) and C II (Figure 1; panel (C)) lines correspond to the chromospheric plasmas, which show evidence of the cool loops. The top part of the loop system is not fully evident in some cool lines; however, its lower part above the footpoints is clearly visible. The loop system along with the different loop strands is clearly identified in the Si IV (Figure 1; panel (D)) line along with its footpoint at both ends.

Various parametric maps for the first data set. We have selected various boxes near the footpoints of these cool loops, which are shown in the left panel of Figure 4 at the Si IV intensity map. Some boxes are located in the blueshifted end (e.g., B1, B2, etc.) while others are located in the redshifted end (e.g., R1, R2, etc.). These locations of the boxes are chosen to have higher emissions such that the intensity along the strand becomes more than double at the footpoint. The averaged spectra for each box is obtained by averaging all existed spectra within the particular box. Similar criteria for the selection of boxes has been followed by other data sets (Data set 2 and Data set 3). Figure 2 presents averaged profiles of different spectral lines used in our analysis. The spectral profiles correspond to the box labeled B5 for Data set 1 (Figure 4). The black solid line represents the averaged spectral profile for different spectral lines where corresponding errors are indicated by the error bars. The red solid line is the fitted profile on the observed profiles (black lines). We have fitted the each observed profiles within ROI to get the intensity, Dopper velocity, and FWHM maps. Left column of Figure 3 shows the intensity (top left), Doppler velocity (middle left) and FWHM maps (bottom left) of the Mg II k. In the similar fashion, we have shown the intensity, Doppler velocity, and FWHM maps of C II 1334.53 Å (middle column) and Si IV 1403.53 Å (right column) in Figure 3. Since Mg II k is an optically thick line, it shows a doubly peaked

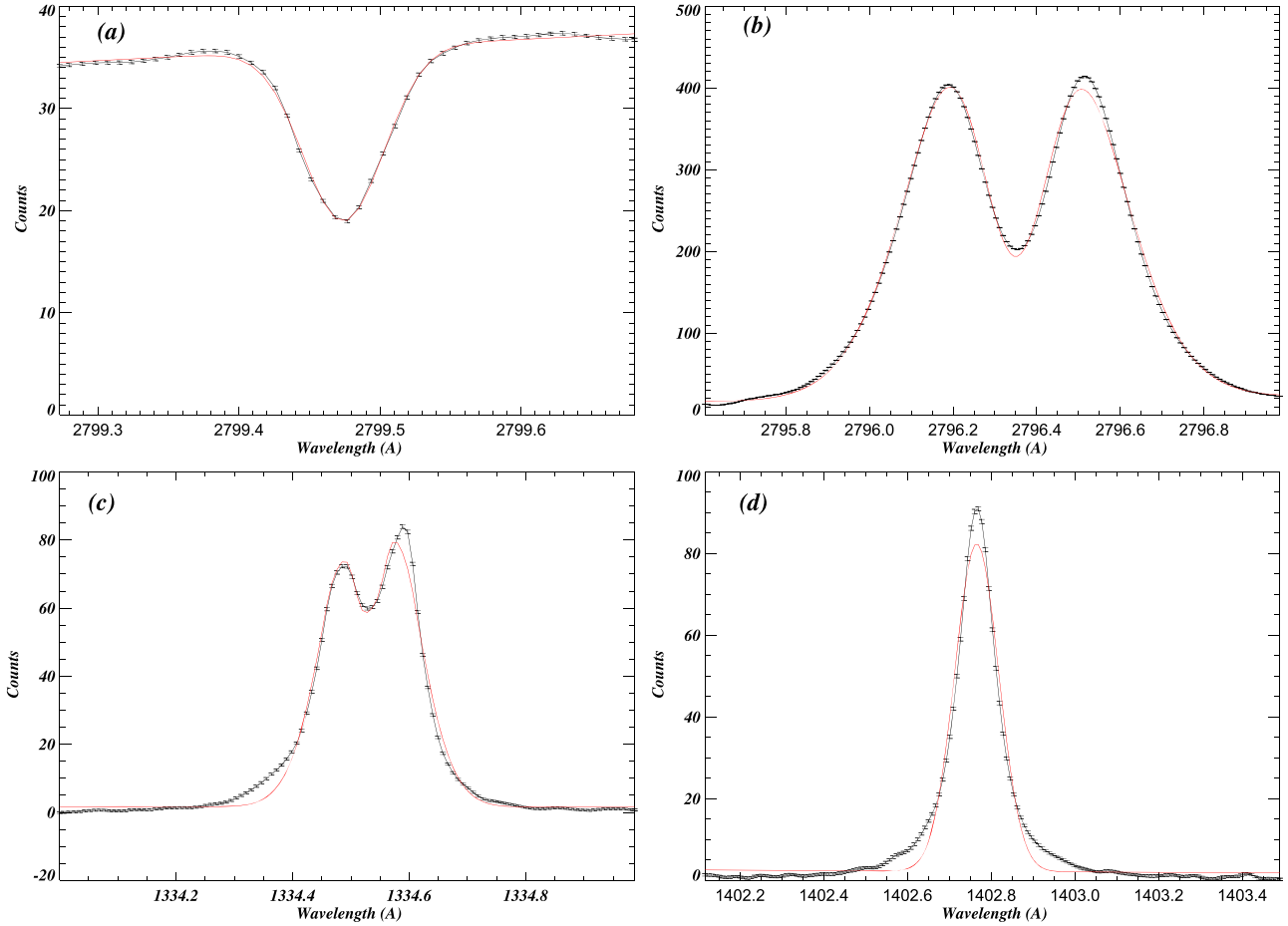

Figure 2. Spectral fitting of (a) Ni I (2799.47 Å), (b) Mg II k (2796.2 Å), (c) C II (1334.53 Å), and (d) Si IV (1402.77 Å) lines for the averaged profile over the box labeled as B5 shown in the Si IV left panel of Figure 4 corresponding to Data set 1.

profile which has been fitted by using two Gaussians (positive and negative). Similar properties hold for the optically thick line C II 1334.53 Å. For Mg II 2796.35 Å and C II 1334.53 Å lines, we have taken the parameters from negative Gaussian, which captures the minima between two peaks. This minima basically forms in the upper chromosphere/TR. For the location exhibiting the single peak, we have taken the same parameters from positive Gaussian because only one Gaussian is present in this case. The detailed description is provided in the Appendix. Using this methodology, we have produced the intensity, Doppler velocity, and FWHM maps for Mg II k and C II lines. The estimation of these maps from the Si IV line is straightforward as the line is a single peak line. For Mg II k, the intensity map (top left panel; Figure 3) shows the loop structures for which the footpoints are not distinct but the top part is clearly visible. Doppler velocity map (middle left panel; Figure 3) shows blueshifted velocities at one end and redshifted at another which has been mapped having values ranging from (−10.0 to +10.0) km s^{-1}. The corresponding FWHM map is shown in the bottom left panel of Figure 3. The line width range for Mg II k varies from (0.10 to 0.35) Å.

For the C II line, such parametric maps are shown in the middle column of Figure 3 where the fuzzier loops are visible (top panel; Figure 3) along with the direction of plasma flow indicated by the Doppler velocity map (middle panel; Figure 3(ii)). The FWHM map of C II 1334.53 Å is displayed in the bottom panel of Figure 3(ii), which has values ranging from 0.05 Å to 0.30 Å. The cool loop system for the Si IV line with different strands is clearly visible in the intensity image (top panel; Figure 3) representing plasma maintained at TR temperature. The corresponding Doppler velocity shows the blueshifted and redshifted opposite footpoints of the cool loop system (Middle panel; Figure 3). The Si IV Doppler velocity map has also been discussed by Huang et al. (2015) targeting the same AR using the Si IV line with different time duration (21:02 UT to 21:36 UTC) corresponding to a different data set. Their results are qualitatively similar to what we have observed in the Doppler velocity map of Si IV line. We have then correlated Doppler velocity maps with FWHM maps for Si IV line as well as some other lines which have been shown in Figure 3. One end of the cool loop system is dominated by redshifts (downflows), while the other end is dominated by blueshifts (upflows). This change from blueshifts at one end to the redshifts at the other end shows the direction of plasma flows. The plasma flow structures are similar to the loop structure visible in the intensity map of the Si IV line (top panel; Figure 3). The blueshifted region shows lower values of FWHM and the redshifted end shows higher FWHM values (bottom panels; Figure 3). The corresponding values of FWHM ranging from (0.05 to 0.25 Å) are shown in the colorbar, which exhibits the characteristics of TR. The increased linewidth at the redshifted (downflows) footpoint may be due to the heating caused by downflowing mass motions there, which are attributed to the line broadening (Tian et al. 2008, 2009).

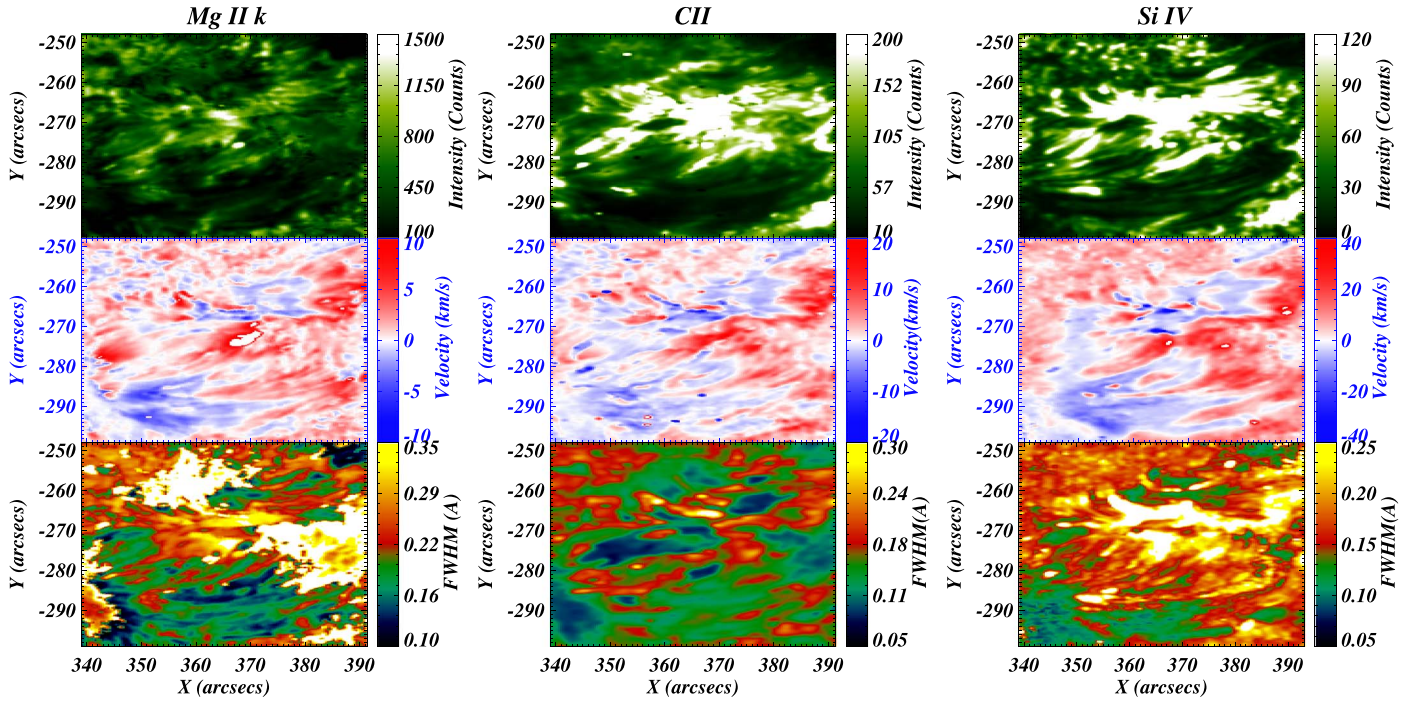

Figure 3. Intensity, Doppler velocity, and FWHM maps of Mg II k (2796.2 Å), C II (1334.53 Å), and Si IV (1402.77 Å) lines are shown for Data set 1 in the left, middle, and right columns, respectively.

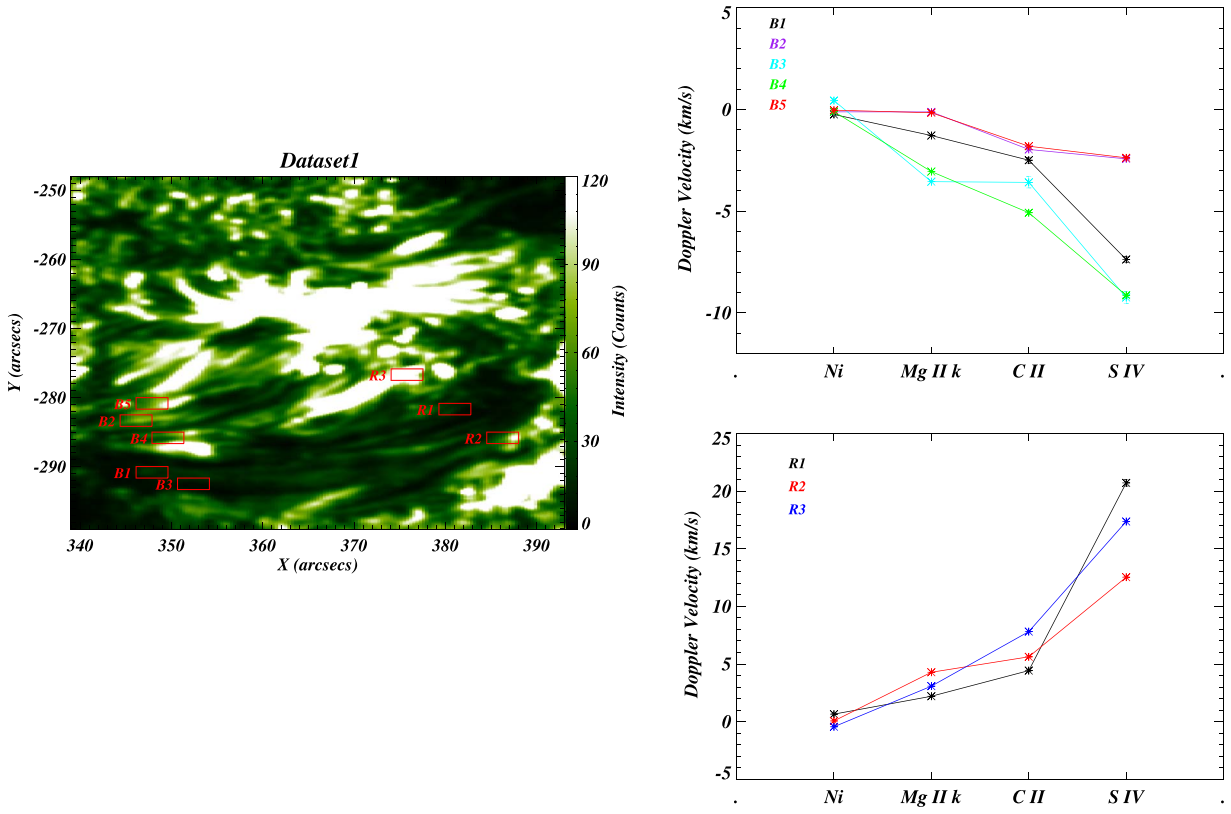

Figure 4. Left panel: the intensity map of Si IV (1402.77 Å) line with the boxes overlaid showing different locations at the footpoints of the cool loop systems. Top right panel: the variation of Doppler velocity with the formation heights of different spectral lines for different boxes at the blueshifted footpoint indicated in the left panel. Bottom right panel: the variation of Doppler velocity with the formation heights of different spectral lines for different boxes at the redshifted footpoint indicated in the left panel.

Variation of Doppler velocity. The boxes overlaid on the intensity map of the Si IV line are labeled B1, B2, B3, B4, B5, and R1, R2, R3 (Left panel; Figure 4). These boxes indicate the locations of the footpoints of different loop strands chosen to investigate the Doppler velocities above the footpoints of the cool loop threads. The average spectral profiles from these

boxes are used to infer qualitatively the Doppler velocity pattern in these regions. The photospheric signature of the footpoints of the loop system in *SDO*/HMI having positive and negative polarities at opposite ends shows almost bipolar magnetic loops. Assuming the loops have similar behavior at the footpoints, plasma flows are investigated using Doppler velocities of multispectral lines. The variation of Doppler velocities is shown in the top right panel of Figure 4 corresponding to the five different boxes (i.e., B1, B2, B3, B4, and B5) at the blueshifted footpoints of cool loop systems as shown in the left panel of Figure 4. The Doppler velocity of the Ni I line is very low in all boxes showing almost no upflows or downflows (−0.24 to 0.44) km s^{-1} in the photospheric region. These blueshifts (upflows) increase for B1, B3, and B4 while they remain nearly the same for B2 and B5 up to the formation temperature of Mg II k. These boxes at formation temperature of Mg II k lines show considerable blueshifts (−0.11 to −3.54) km s^{-1}. However, the significant change in the blueshifts occurs at the formation temperature of C II for the different boxes as revealed by the top right panel of Figure 4. The Doppler velocity variation at Si IV shows blueshifts having −2.42 and −2.37 km s^{-1} value for B2 and B5 while B1, B3, and B4 have high blueshifts (i.e., −7.37 km s^{-1}–B1, −9.24 km s^{-1}–B2, and −9.14 km s^{-1}–B4).

We have also considered three locations labeled R1, R2, and R3 in the redshifted region within the other footpoints of this cluster of cool loops. The Doppler velocities increase for different spectral lines showing the increase in plasma downflows as we go higher up in the solar atmosphere as shown in the bottom right panel of Figure 4. The Doppler velocity for the Ni I line shows small flows having the range (−0.44 to 0.64) km s^{-1} for different locations. The optically thick lines (Mg II k and C II) are fitted as discussed in the Appendix. The centroid of the negative Gaussian is used to estimate the corresponding Doppler velocities, which range from the middle chromosphere to the upper chromosphere. The Mg II k line has significant downflows with a Doppler velocity range of (2.20–4.42) km s^{-1}. The downflows are then increased as we go higher to the formation height of C II having a Doppler velocity range of (4.28–7.81) km s^{-1}. These values reach the maximum values of (12.53–20.72) km s^{-1} for the Si IV line, which is formed in the TR. The maximum activity is found in the upper chromosphere/TR interface where the downflows become large and create excess widths at the associated footpoints. The corresponding 1σ error in the line centroid of the fitted profile converted into velocity terms has been shown in terms of error bars for different lines at different positions. The 1σ velocity error being very small, it is hard to visualize these errors in the corresponding figures (see Figure 4).

Line widths of Si IV at red- and blueshifted footpoints of cool loops. We have also investigated the FWHM of the Si IV line within all boxes (blue as well as red) for the first data set. The FWHMs of the blue boxes of the first observation are 0.095 Å (B1), 0.127 Å (B2), 0.114 Å (B3), 0.153 Å (B4), and 0.123 Å (B5), while the red boxes have widths of 0.215 Å (R1), 0.185 Å (R2), and 0.246 Å (R3).

Thermal width ($\sigma_{\rm th}$) of the Si IV line is 0.09 Å, while the instrumental width ($\sigma_{\rm inst}$) is 0.026 Å (De Pontieu et al. 2014). Therefore, the nonthermal component of the line widths ($\sigma_{\rm nt} = (\sigma^2_{\rm obs} - \sigma^2_{\rm th} - \sigma^2_{\rm inst})^{1/2}$) derived by the averaged spectral line profiles at different blueshifted boxes (B1–B5) ranges between 0.015 and 0.120 Å. The plasma upflow is also associated with these regions of increased nonthermal width. In the present observational baseline, we conjecture the presence of localized energy release due to small-scale magnetic reconnection above the footpoints of the cool loop threads, and filling-up of the evaporated plasma in these threads that we observe in the form of the blueshift (e.g., Patsourakos & Klimchuk 2006; Hansteen et al. 2014; Huang et al. 2015; Polito et al. 2015).

It is obvious that the redshifted footpoints have higher line widths (almost double) compared to the blueshifted footpoints. The downfall or condensation of the cool-loop plasma toward their redshifted footpoints in TR may contribute to the line width broadening (Tian et al. 2009). There may be additional physical processes that may cause excess line broadening on the redshifted TR footpoints of the loop system, *viz.*, nanoflare generated acoustic waves (Hansteen 1993) from the overlying atmosphere, overall downward propagating pressure disturbances (Zacharias et al. 2018), etc.

3.2. Data Set 2

Identification of cool loops. The middle column of Figure 1 shows the region of interest consisting of a cool loop system for Data set 2 along with the magnetic polarities at the footpoints shown by the LOS magnetogram (Figure 1; panel (E)). The observational signatures of the existence of the cool loop system are shown using Mg II k (Figure 1; panel (F)), C II (Figure 1; panel (G)), and Si IV (Figure 1; panel (H)) line intensity maps. The intensity map of the Si IV line (Figure 1; panel (H)) shows faint loops corresponding to the temperatures of the TR. The characteristic behavior of the loop system for different spectral lines is similar to that of the description for Data set 1 (left column; Figure 1).

Parametric maps for the second data set. Figure 5 represents average observed profiles (averaged over the selected boxes B4) of different spectral lines. The displayed spectral profiles correspond to the box labeled B4 for Data set 2 (left panel; Figure 7). Figure 6 shows the intensity, Doppler velocity, and FWHM maps for Mg II k (Figure 6; left column), C II (Figure 6; middle column), and Si IV (Figure 6; right column). The Doppler velocity maps (middle panel in each column; Figure 6) show that one of the footpoints is redshifted while the other is blueshifted. The upflowing plasma (i.e., the blueshifted end) is falling to the other end, which causes redshifts there. The corresponding values of Doppler velocity are shown by the colorbars in each panel. The line widths are represented by FWHM maps in the bottom panels of Figure 6 for Mg II k3 (left-cloumn), Figure 6 for C II (middle column), and Figure 6 for Si IV (right column), where the increased linewidth at the redshifted footpoint might be due to downflowing plasma (Tian et al. 2008, 2009).

Variation of Doppler velocity. The locations used for Doppler velocity estimations are labeled as B1, B2, B3, B4, B5, B6 and R1, R2, R3 at the blueshifted and redshifted footpoints of the cool loop system for Data set 2 shown in the left panel of Figure 7. The top right panel shows the variation of Doppler velocity for Data set 2 at the blueshifted footpoints of the cool loop system for boxes shown in the left panel of Figure 7. The Doppler velocity of the Ni I line is very low in all boxes showing almost no upflows or downflows (−0.07 to 0.44) km s^{-1} in the photospheric region. These flows show small redshifts/blueshifts for selected different boxes at the formation temperature of Mg II k. All these flows show considerable blueshifts (−0.50 to −2.74) km s^{-1} at C II. The

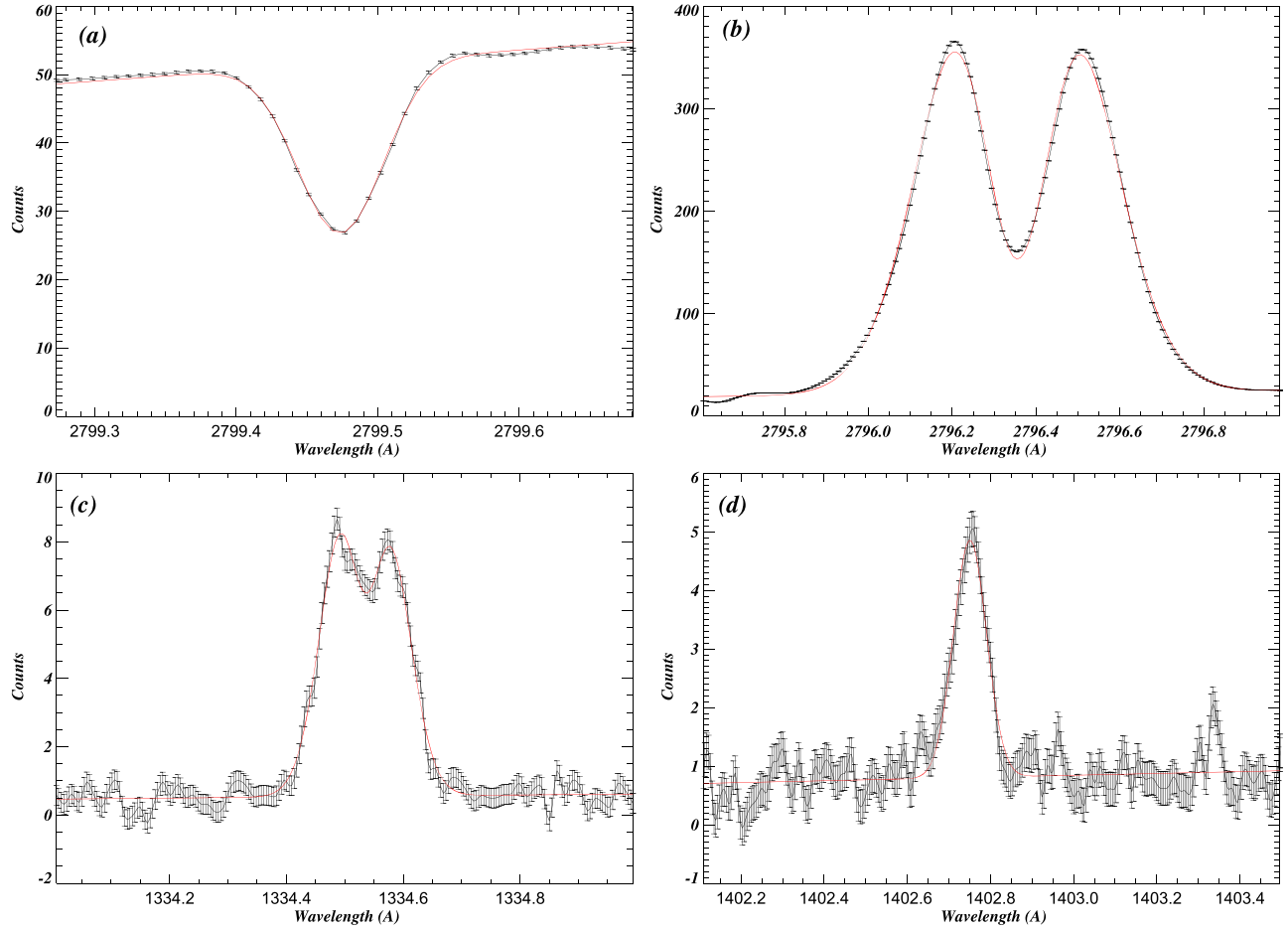

Figure 5. Spectral fitting of (a) Ni I (2799.47 Å), (b) Mg II k (2796.2 Å), (c) C II (1354.5 Å), and (d) Si IV (1402.77 Å) lines for averaged profile over the box labeled as B4 shown in the left panel of Figure 7 corresponding to Data set 2.

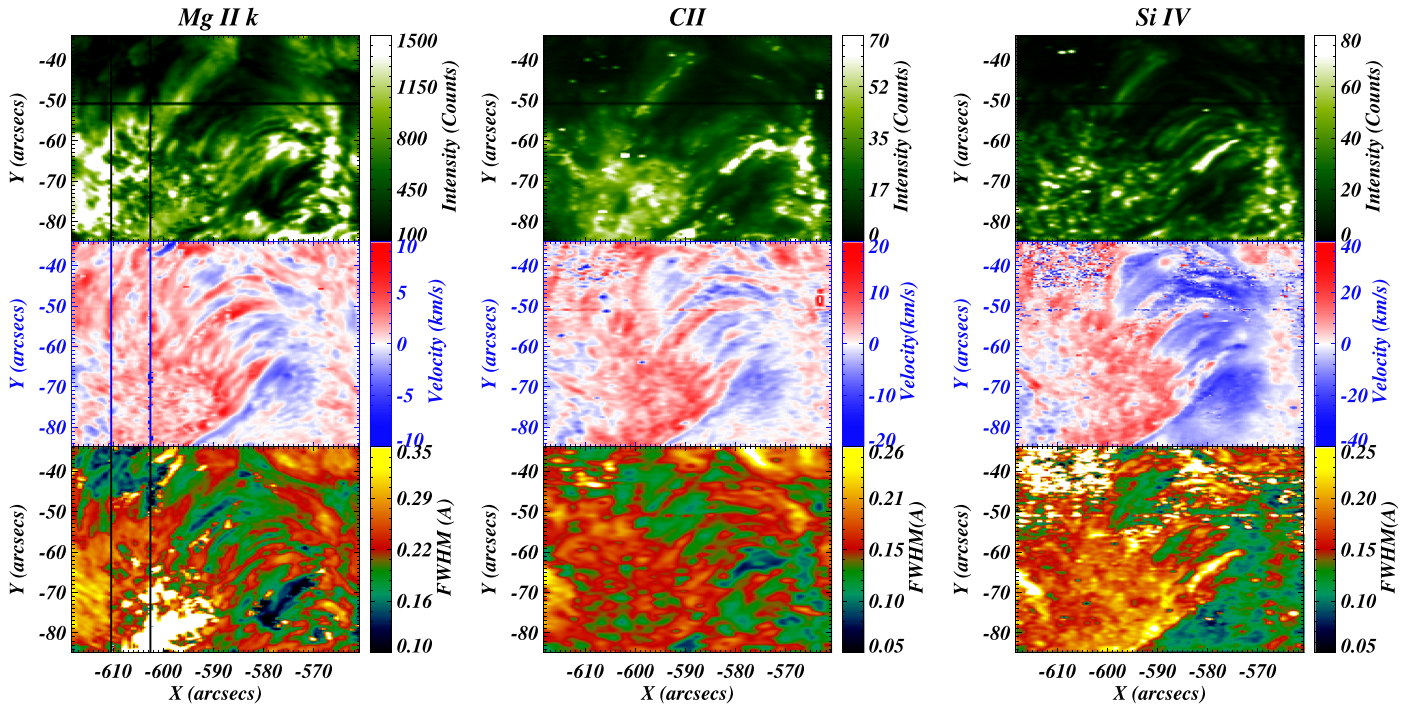

Figure 6. Intensity, Doppler velocity, and FWHM maps of Mg II k (2796.2 Å), C II (1334.53 Å), and Si IV (1402.77 Å) lines are shown for Data set 2 in the left, middle, and right columns respectively.

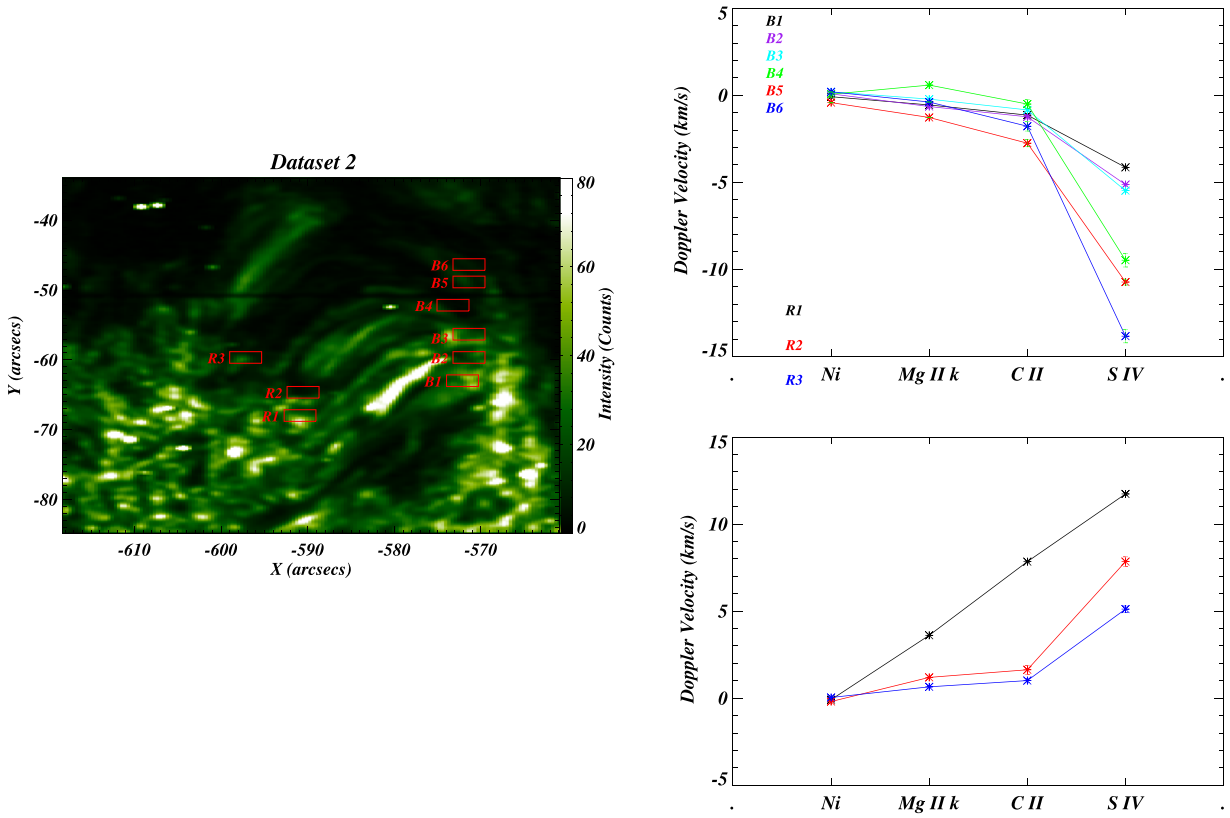

Figure 7. Left panel: the intensity map of the Si IV (1402.77 Å) line with the boxes overlaid showing different locations at the footpoints of the cool loop systems. Top right panel: the variation of Doppler velocity with the formation heights of different spectral lines for different boxes at the blueshifted footpoint indicated in the left panel. Bottom right panel: the variation of Doppler velocity with the formation heights of different spectral lines for different boxes at the redshifted footpoint indicated in the left panel.

Doppler velocity at Si IV shows high blueshifts for B4, B5, and B6 having a maximum value of -13.83 km s^{-1}. However, the boxes B1, B2, and B3 show relatively small upflows with velocity (-4.13 to -5.47) km s^{-1}. The corresponding error bars (1σ error) are overplotted; however, they are not visible due to their very small amplitudes.

We have also considered three locations within the redshifted footpoints of this cluster of cool loops, which are labeled as R1, R2, and R3. The Doppler velocities increase for different spectral lines showing the increase in plasma downflows as we go higher up in the solar atmosphere as shown in the bottom right panel of Figure 7. The Doppler velocity for the Ni I line shows small flows with the range (-0.08 to 0.04) km s^{-1}. The Mg II k line has relatively small downflows with a Doppler velocity range of (0.65–3.61) km s^{-1}. The downflows are then increased as we go higher to the formation height of C II with a Doppler velocity range of (1.01–7.84) km s^{-1}. These values reach maximum values of (5.11–11.73) km s^{-1} for the Si IV line. The maximum activity is found in the upper chromosphere/TR interface, where the downflows become large and create excess widths at the associated footpoints.

Line widths of Si IV *at red- and blueshifted footpoints of cool loops.* We have also investigated the FWHM of the Si IV line within all boxes (blue as well as red) for the second data set. FWHM of the blue boxes of the second observation is 0.107 Å (B1), 0.105 Å (B2), 0.108 Å (B3), 0.094 Å (B4), and 0.131 Å (B5), and 0.141 Å (B6). While, the red boxes have widths of 0.200 Å (R1), 0.186 Å R2), and 0.187 Å (R3) indicating higher line widths at the redshifted locations. A similar trend of FWHM in blue and red boxes is also found in this observation as Data set 1; therefore, the possible physical implications remain the same.

3.3. Data Set 3

Identification of cool loops: The right column of Figure 1 shows the mosaic of the intensity images for different spectral lines for Data set 3 along with the magnetic polarities at the footpoints shown by the LOS magnetogram (Figure 1; panel (I)). The loop strands are visible as clearly resolved structures in Si IV line intensity (Figure 1; panel (L)) while Mg II k (Figure 1; panel (J)) and C II (Figure 1; panel (K)) show chromospheric/TR signatures and the loop strands appear fuzzier. The loop structures are thus shown at different wavelengths corresponding to different formation heights in the solar atmosphere. The LOS magnetogram indicates the opposite magnetic polarities at the footpoints of the cool loop system.

Parametric maps for the third data set. Figure 8 represents average profiles of different spectral lines corresponding to the box labeled B3 for Data set 3 (left panel; Figure 10). Figure 9 shows the intensity, Doppler velocity, and FWHM maps for Mg II k (Figure 9; left column), C II (Figure 9; middle column), and Si IV line (Figure 9; right column). The plasma emissions in the intensity maps (top panels; Figure 9) are similar to the direction of plasma flows in the Doppler velocity maps (middle panels; Figure 9) having blueshifts at one end and redshifts at the other end. The linewidths in the bottom panels of Figure 9 show the mass motion signatures of the plasma having high

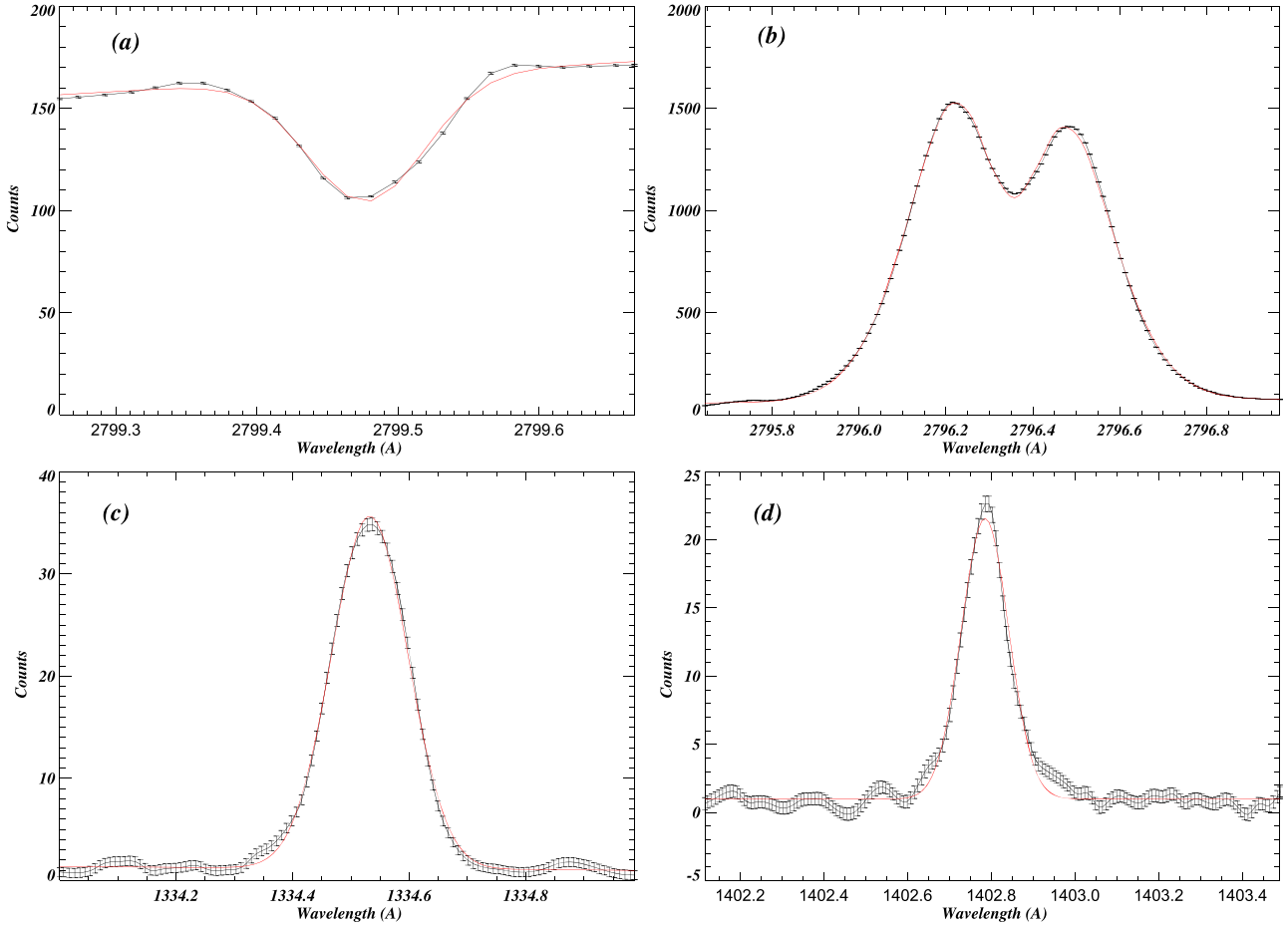

Figure 8. Spectral fitting of (a) Ni I (2799.47 Å), (b) Mg II k (2796.2 Å), (c) C II (1334.53 Å), and (d) Si IV (1402.77 Å) lines for box labeled as B3 in the left panel of Figure 10 for Data set 3.

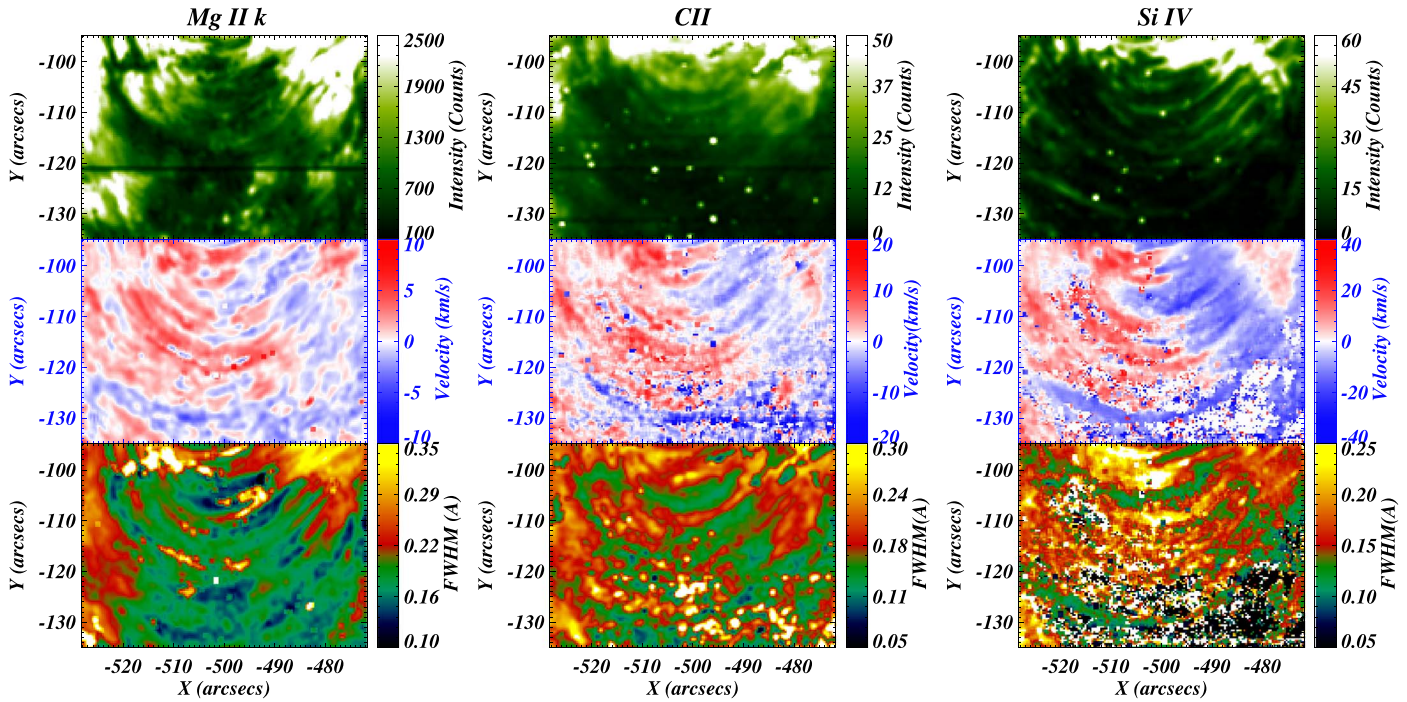

Figure 9. Intensity, Doppler velocity, and FWHM maps of Mg II k (2796.2 Å), C II (1334.53 Å), and Si IV (1402.77 Å) lines are shown for Data set 3 in the left, middle, and right columns, respectively.

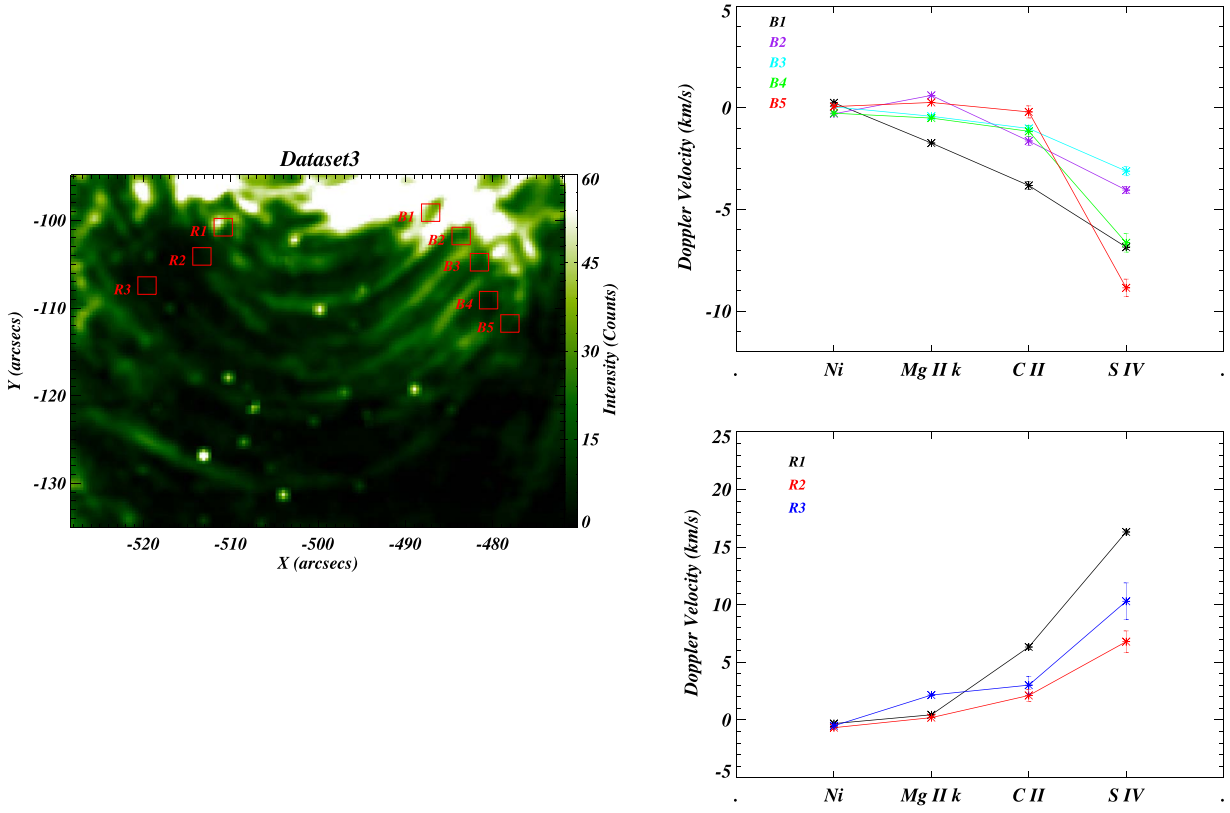

Figure 10. Left panel: the intensity map of Si IV (1402.77 Å) line with the boxes overlaid showing different locations at the footpoints of the cool loop systems. Top right panel: the variation of Doppler velocity with the formation heights of different spectral lines for different boxes at the blueshifted footpoint indicated in the left panel. Bottom right panel: the variation of Doppler velocity with the formation heights of different spectral lines for different boxes at the redshifted footpoint indicated in the left panel.

values of FWHM at the redshifted footpoint indicating the heating caused by downfalling plasma (Tian et al. 2008, 2009).

Variation of Doppler velocity. In Figure 10, the top right panel shows the variation of Doppler velocity for Data set 3 at the blueshifted footpoints of the cool loop system for boxes shown in Figure 9. The Doppler velocity of the Ni I line is very low in all boxes showing almost no upflows or downflows (-0.05 to -0.28) km s^{-1} in the photospheric region. These flows show small redshifts and blueshifts for different boxes at the formation temperature of Mg II k lying in the range (-1.72 to 0.61) km s^{-1}. Interestingly, all these boxes show considerable blueshifts (-0.19 to -3.81) km s^{-1} at C II. The Doppler velocity variation at Si IV shows high blueshifts for the maximum value of -8.84 km s^{-1} for B5.

In a similar fashion as we did in the previous cases, we have also considered three boxes in the redshifted region near other footpoints of this cluster of cool loops. The redshifts increase for different spectral lines showing the increase in plasma downflows as we go higher up in the solar atmosphere as shown in the bottom right panel of Figure 10. The maximum activity is found in the upper chromosphere/TR interface where the downflows become large and create excess widths at the associated footpoints. The variation of Doppler velocities above redshifted footpoints for different boxes (R1, R2, and R3) shows the increasing trend as observed in previous data sets for downflowing velocities at different formation heights of the spectral lines where the maximum values reaches the formation height of Si IV with the Doppler velocity range (6.79–16.31) km s^{-1}.

Line widths of Si IV at red- and blueshifted footpoints of cool loops. We have also investigated the FWHM of the Si IV line within all boxes (blue as well as red) for the third data set. The FWHM of the blue boxes of the third observation is 0.149 Å (B1), 0.135 Å (B2), 0.134 Å (B3), 0.125 Å (B4), and 0.126 Å (B5), while the red boxes have widths of 0.182 Å (R1), 0.139 Å R2), and 0.172 Å (R3). Possible physical explanations for such excess width have already been mentioned for Data sets 1 and 2.

4. Discussions and Conclusions

We have studied various cool loop systems in order to understand the cospatial variations of Doppler velocities at various locations with blueshifted footpoints as well as redshifted footpoints for different spectral lines having different formation heights. The Doppler variation shows the increasing height trend in the solar atmosphere.

The photospheric, as well as chromospheric, regions show very small blueshifts of $\sim$(+1 to -1) km s^{-1}, which exhibit almost no upflow signatures until Mg II k. On the contrary, the C II lines are significantly blueshifted by $\sim$(-1 to -6) km s^{-1}. The blueshifted nature becomes more prominent at the formation temperature of Si IV. In Data set 1 and Data set 2, upflows are indicated above C II formation height at the blueshifted footpoints, which is well supported by the downflowing plasma at the redshifted footpoints. However, for Data set 3, these upflows start below C II formation height (upper chromosphere) and are then driven by plasma inertia to higher heights until Si IV, and show small downflows at C II at

redshifted footpoints. All the blueshifted locations for the same data set follow similar patterns but have different ranges of Doppler velocities showing the localized impulsive events. These flows are initiated by short impulsive events that are highly localized in the upper chromosphere or lower TR. Such localized impulsive events above or below the C II formation height make the loops thermally unstable.

Thus the significant plasma upflows take place between the formation heights of C II and Si IV lines for Data set 1 and Data set 2, while it takes place below the formation heights of C II. The transition of small upflow to high upflow velocities takes place near the formation height of the C II line, which justifies the origin site of plasma flow in these cool loops.

Different plausible mechanisms have already been discussed for the origin of flows in coronal loops, e.g., siphon flow (Hood & Priest 1981), downward propagating acoustic waves (Hansteen 1993), explosion below corona (Teriaca et al. 1999), acoustic waves (Taroyan et al. 2005), and nanoflare driven chromospheric evaporation (Patsourakos & Klimchuk 2006). However, the occurrence of implusive heating involving magnetic reconnection has recently been reported in support of the plasma flows in the cool loop systems (Huang et al. 2015).

Warren et al. (2002) have suggested the impulsive heating of active region hot loops using *TRACE* observations. Spadaro et al. (2003) have also explained the flows in the coronal loops due to transient heating near the chromsophere. The outflow locations at the footpoints in cool loop systems have higher emissions indicating the dynamical nature of the loops. Localized impulsive energy release might be driving such flows because there are no flows at a few footpoints of the cool loop system (B1, B2, B3; Figure 7) while other footpoints near it show upflows. The heating due to impulsive energy release gets deposited at that footpoint to drive the upflows. That portion of the flowing plasma arriving at the opposite footpoint, causes an enhancement of the linewidth. Thus, the speculation of such loop systems driven by heating pulses due to magnetic reconnection is supported by our observations. The nonthermal broadening of the Si IV line at the blueshifted footpoints of the cool-loop system is most likely associated with the ongoing transient energy release and thereafter filling-up of the plasma in loop threads (e.g., Patsourakos & Klimchuk 2006; Hansteen et al. 2014; Huang et al. 2015; Polito et al. 2015). Redshifted footpoints in the Si IV line indicate that the TR plasma is flowing down on the other end of the loop system, and the excess nonthermal width may be associated with the variety of physical processes there, e.g., downfalling of the plasma (Tian et al. 2009), nanoflare generated acoustic waves (Hansteen 1993), downward propagating pressure disturbances (Zacharias et al. 2018), etc. The exact answer is still an open question exploring what physical process(es) causes these TR footpoints of the cool loop threads with excess line width.

Since the transition of plasma upflows starts at the TR (near the C II line formation height), they can transport mass and energy directly to the inner corona above the cool loop systems. Therefore, such loop systems play a significant role in the mass, energy, and momentum transport. They may be the lower counterparts of high temperature coronal loops. High speed plasma flows in the magnetic domain of the loops have been observed in the solar atmosphere (Harra et al. 2008). However, there are several unclear propositions regarding the origin of such fast flows. The possible transport of the plasma from the low-lying cool loop systems (the one we observed) to the higher magnetic field configuration where the plasma acceleration starts, may be the most likely source. Such plasma flows, after their acceleration in the higher atmosphere, may provide the plasma for the solar wind, if the open field lines exist in the vicinity of the footpoints of such loops; though, such an example has not been observed in our case.

In conclusion, our work emphasizes the significance of plasma flows at different formation heights of the spectral lines corresponding to different regions of the solar atmosphere in a cool loop system. The height-dependent trend of the Doppler velocities explores the region where these flows start to show prominent upflows. Such flows do not start from the photosphere. On the contrary, they start from the upper chromosphere and TR where transitions from small blueshifts to significantly high blueshifts have been identified in such a system. Future investigations would be required for comparing the Doppler velocity patterns in cool and hot coronal loops using multiline spectroscopy in order to differentiate the underlying causes and different origins of the plasma flows there.

We thank the referee for constructive comments that improved the manuscript. Y.K.R. is fully supported by a financial grant from the ISRO RESPOND project. A.K.S. acknowledges a UKIERI project grant. P.K. acknowledges the grant Rozvoj JU—Mezinarodni mobility–CZ.02.2.69/0.0/16_027/0008364. We acknowledge the use of *IRIS* observations. *IRIS* is a NASA small explorer mission developed and operated by Lockheed Martin Solar and Astrophysics Laboratory (LMSAL) with mission operations executed at NASA Ames Research Center and major contributions to downlink communications funded by the Norwegian Space Center (NSC, Norway) through an ESA PRODEX contract.

Appendix
Fitting Note on Optically Thick Lines

Mg II k 2796.35 Å and C II 1334.53 Å are optically thick spectral lines, which can have single or double peaks or even more (see Figure 12; Leenaarts et al. 2013; Rathore et al. 2015). In the present observations, we have found that a major fraction of Mg II k 2796.35 Å has double peak profiles (i.e., k2v and k2r) with associated minimum between these two peaks (i.e., k3). However, in the case of sunspot umbra the Mg II k are single peak profiles as reported by Tian et al. (2014). We have used two Gaussian (one positive and another negative) along the straight line to fit the Mg II k 2796.35 Å line. Our fitting model is similar to the one used by Schmit et al. (2015). We have used a straight line to fit the continuum while Schmit et al. (2015) have used a polynomial.

Figure 11 shows some sample fittings from various features within the observed region (i.e., Data set1). Typical single peak profiles exist in the sunspot umbra (panel (a)) while a slight dip is visible within the penumbra atmosphere (panel (b)). We have shown the chi-squared value and the fitting parameters (positive Gaussian (black) and negative Gaussian (blue)) in each plot. However, in other features (i.e., QS, high-intensity regions (plages), and loops) the Mg II k profiles are the typical double peak profiles (panels (c), (d), (e), and (f)) as also reported in previous *IRIS* related works (Carlsson et al. 2015; Schmit et al. 2015; Kayshap et al. 2018). In the case of panel (e), the profile comes from very high intensity/activity regions, which have high chi-square values. However, the observed

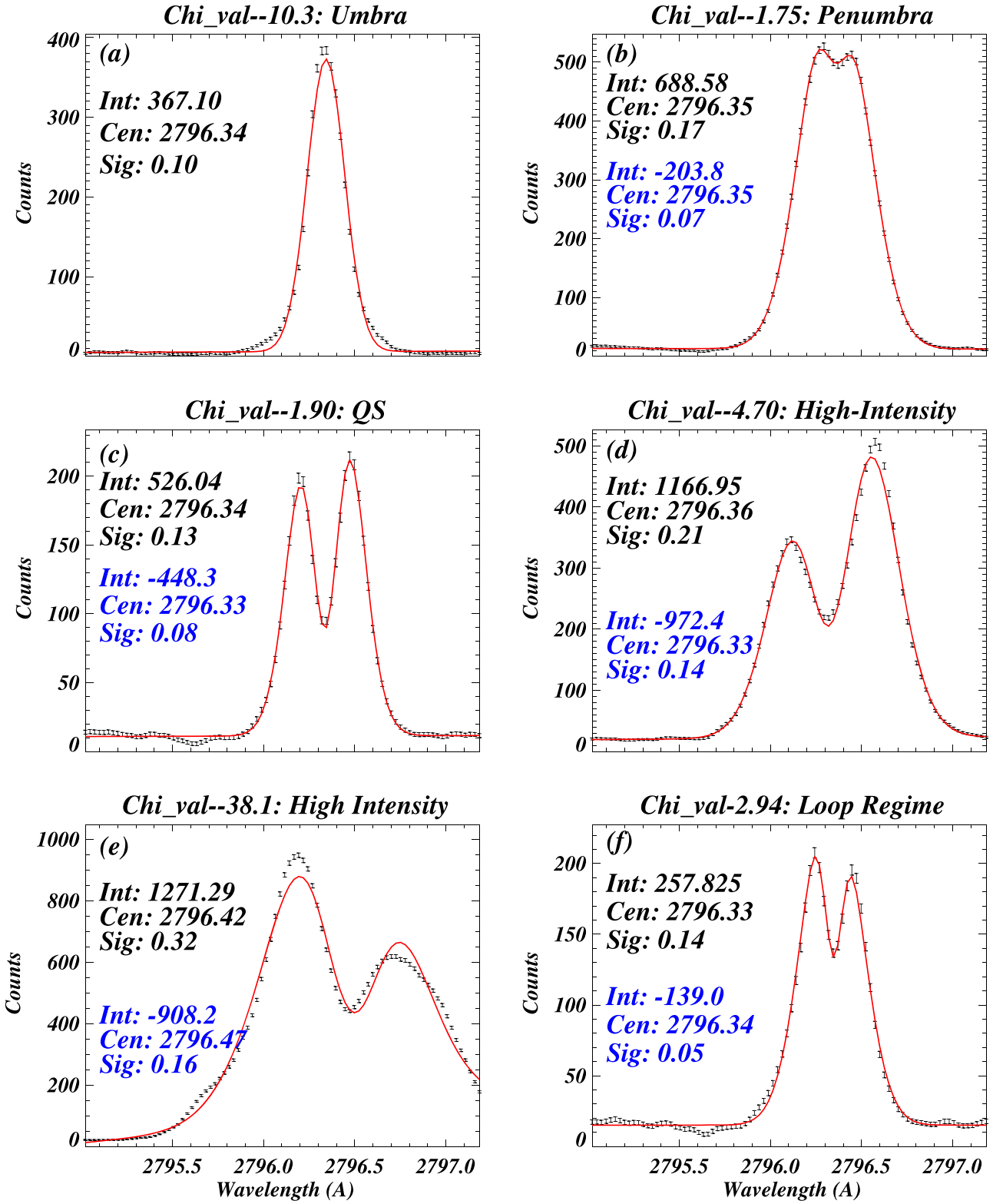

Figure 11. Samples of our fitting model on the observed profiles of Mg II k 2796.35 Å within the different features, e.g., umbra (panel (a)), penumbra (panel (b)), QS (panel (c)), high-intensity (panels (d) and (e)), and loop regime (panel (f)). The black line shows the observed profiles while the red line is the fitted model on the observed profiles. We have also displayed the parameters (peak intensity, centroid, and Gaussian sigma) from positive Gaussian (black) and negative Gaussian (blue) in each panel. These samples illustrate the variations of the Mg II k line within the different features in the observed region. The fitting model captures the line behavior very well, which justifies our fitting model for the Mg II k line.

profiles are well characterized by the fitting model. In the rest of the cases, the chi-square values are in good agreement. Some very complex spectral profiles also exist, which are shown in Figure 12. These complex spectral profiles have three or more peaks, which cannot be characterized with the present model (see fitted red lines on the observed profiles; Figure 12).

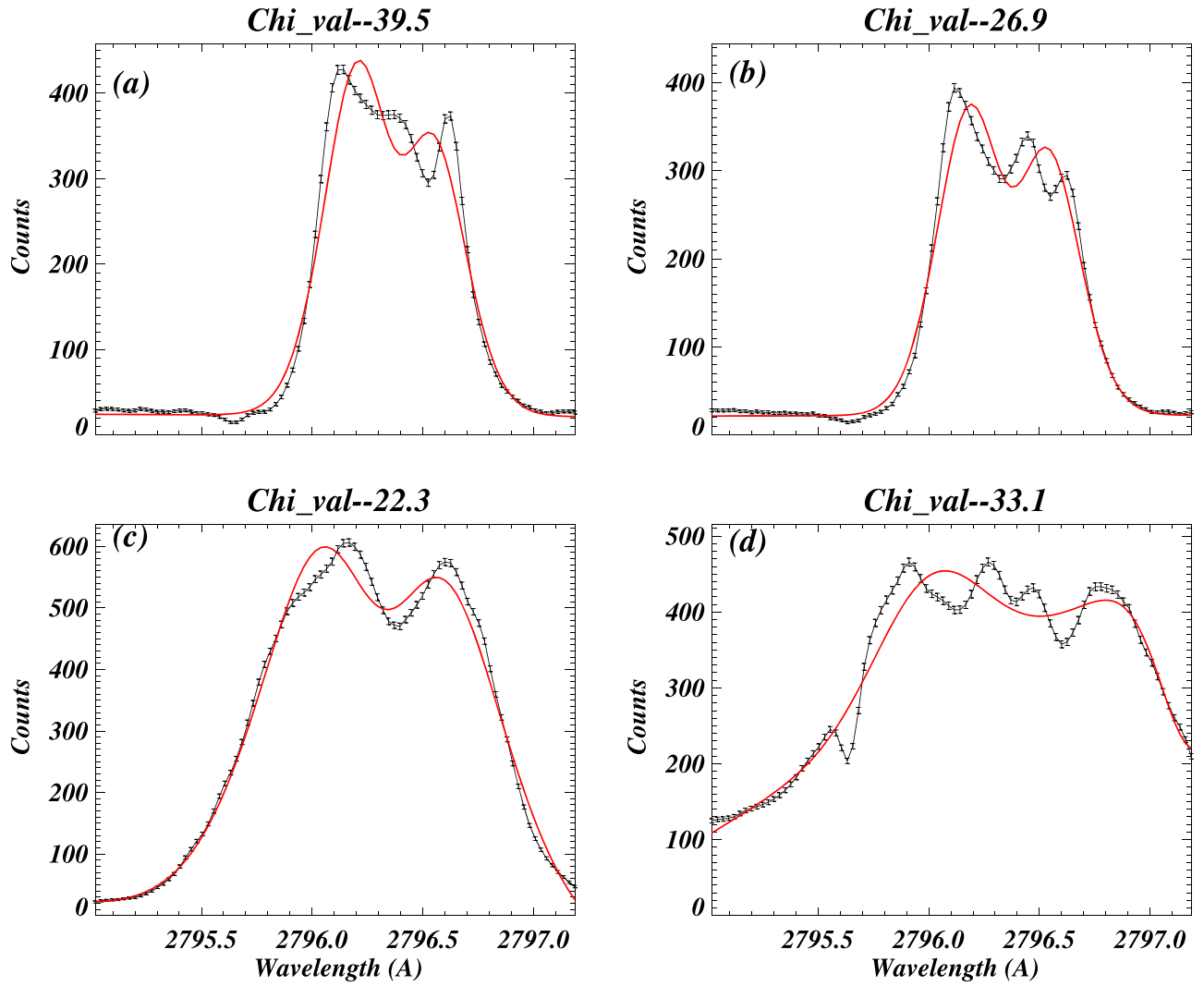

Figure 12. In this figure, we have shown some very complex Mg II k profiles occurring in Data set 1. These complex profiles have 3, 4, or 5 peaks, which cannot be fitted with the current fitting model. However, these profiles are very rare and we did not pursue them in our further analysis.

However, it should be noted that such profiles are very rare in the present observations. Therefore, we have not considered such profiles in our analysis. We have estimated the chi-squared value for each spectral profile in all three observations. The statistical distribution of chi-square values of Mg II k 2796.35 Å is shown in panel (a) of Figure 14. It is clearly visible that the chi-square value is less than 10.0 for most of the spectral profiles, which justify our fitting model for Mg II k 2796.35 Å. Similar types of chi-square distributions are also found for other data sets (Data set 2 and Data set 3), which are not shown here.

Two resonance C II lines (C II 1334.53 Å and C II 1335.71 Å) are present in the *IRIS* FUV filter observation. In general, C II 1335.71 Å is stronger than C II 1334.53 Å; however, the stronger line is blended with another nearly present C II 1335.66 Å line. Therefore, we have used weak but clean C II 1334.53 Å in the present analysis. Considering C II lines as already discussed, we have used the same fitting model as for Mg II k 2796.35 Å double peak profiles. The single peak profiles are fitted by single Gaussian. We have used the averaged spectral profile (with ±1 at every pixel location) as the exposure time is very low in these observations, so the counts are low in this line. We have some sample spectral fitting for Mg II k 2796.35 Å and C II 1334.532 Å lines. However, it should be noted that the C II 1334.53 Å spectral line (weak but clean) has more single peaks (i.e., panel (a): umbra, panel (b): penumbra, panel (c): QS, and panel (f): loop regime) compared to the C II 1335.77 Å line (Rathore et al. 2015). Figure 13 shows some spectral profiles from various features (as we show in the case of Mg II k; Figure 11) from the Data set 1 observation. However, the double peak nature of the C II 1334.53 Å line becomes prominent in the high-intensity regions (panels (d) and (e)). We have found that almost 8% of profiles are double peaked profiles, which are present mostly in the high intensity areas. The chi-square distribution of C II 1334.53 Å fitting, which is shown in panel (b) of Figure 14. We find that the chi-square value is less than 2.0 for the majority of profiles. The similar type of chi-square distributions is found for other data sets (i.e., Data set 2 and Data set 3), which are not shown here.

We have used negative Gaussian for the estimation of Doppler velocity and FWHM for these optically thick lines. In this fitting model, the negative Gaussian basically captures the dip region in between two peaks. The dip region is formed higher up in the chromosphere (Leenaarts et al. 2013; Rathore et al. 2015). As already noted, these optically thick lines can

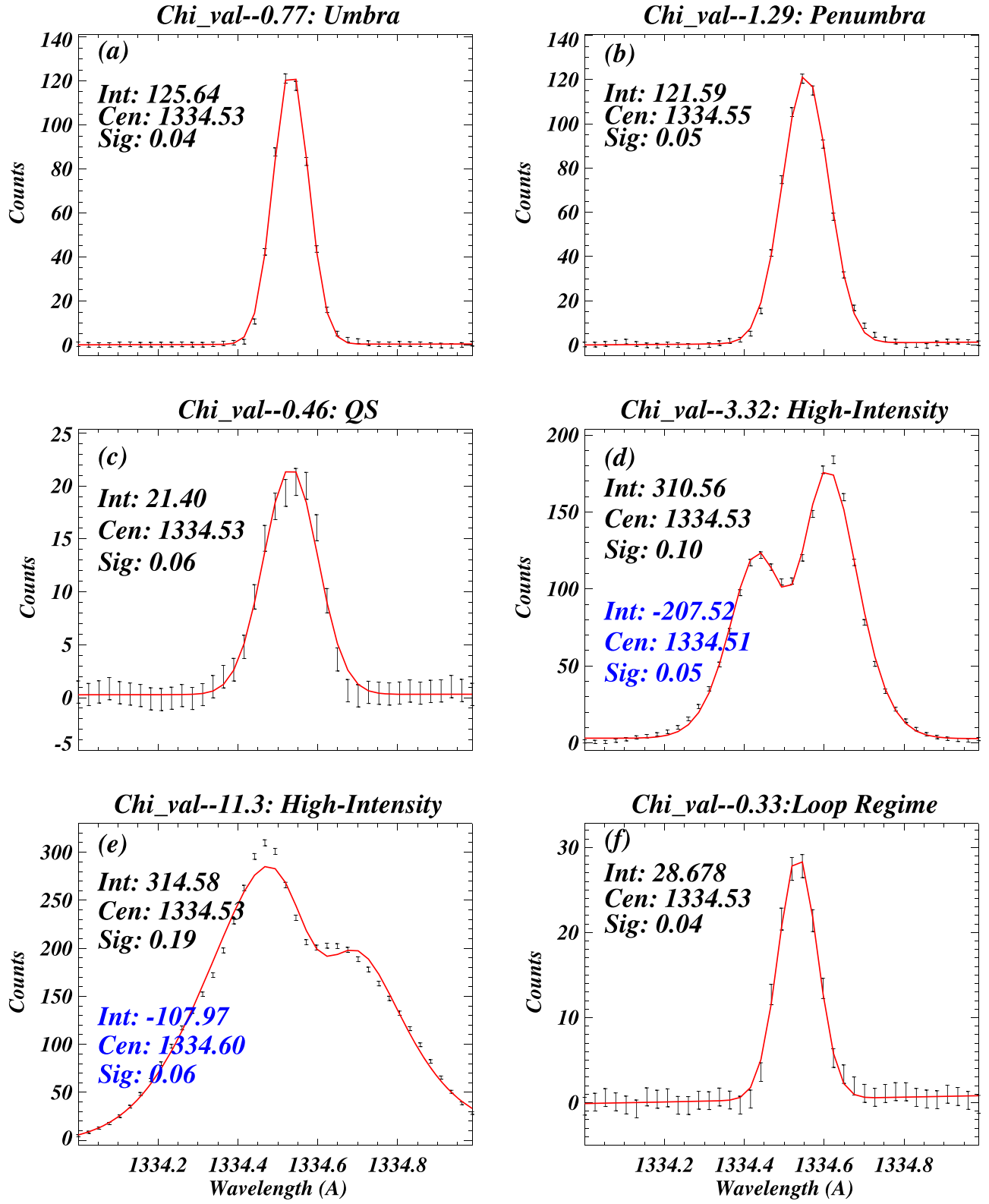

Figure 13. Sample profiles along with their fitting as shown in Figure 11 but for C II 1334.53 Å. Interestingly, C II 1334.53 Å has single peak profiles in all features except for the high-intensity area of the observations. The low value of chi-square justifies the reliability of our fitting model for C II 1334.53 Å.

also have single peak profiles (specifically, C II 1334.532 Å line). Therefore, we do not have the negative Gaussian parameters there. Thus the parameters from single Gaussian (as profiles are single peak) are used at those locations to create the corresponding intensity, Doppler velocity, and FWHM maps (see Figures 3, 6, and 9). Since negative Gaussian captures the variations of the minimum region (dip) between two peaks, the spectral distance between k2v and k2r also varies as per the nature of spectral profiles. The negative Gaussian captures the activity of dip regions, therefore, this

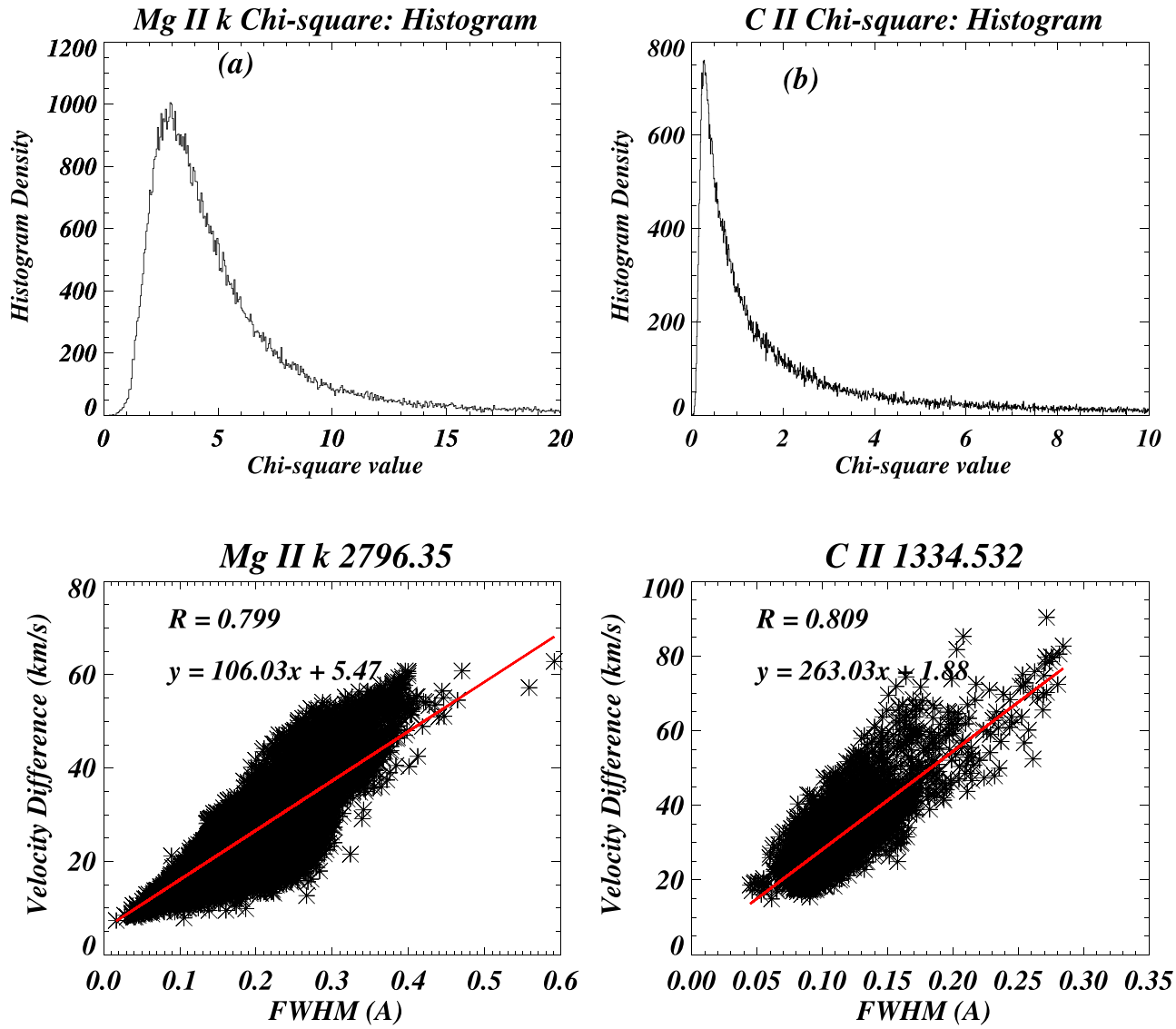

Figure 14. Panel (a) shows the distribution of chi-square values for Mg II k, which are estimated for each fitted profile within Data set 1. Statistical distribution peaks around 3.0 with its major extension up to 12, which shows that the majority of profiles are fitted very well with the current model. Similarly, panel (b) shows the similar chi-square distribution for C II. It peaks around 1 with its major extension up to 5 justifying the fitting of the C II line also. In the bottom left panel, we have shown the correlation between velocity difference (i.e., k2r–k2v) and FWHM of negative Gaussian. We have found a very tight correlation between velocity difference and FWHM. Similarly, the bottom right panel shows the same correlation but for C II, which is also very tight.

spectral distance (k2r and k2v) should reflect in the width of (i.e., FWHM) of negative Gaussian. Therefore, we should expect the positive correlation between the spectral distance between k2r and k2v (or the Doppler velocity difference) FWHM of negative Gaussian. Schmit et al. (2015) have estimated different widths for Mg II h 2803.53 Å, i.e., distance between h1v and h1r and distance between h2v and h2r. They have fitted positive as well as negative Gaussian on the observed profiles using the fitting model (fitted profile) to draw the various peaks and dips (i.e., h1v, h1r, h2v, h2r, and h3) from the fitting model. They have then estimated these two types of width (i.e., h1r–h1v and h2r–h2v). To validate our analysis, we have also used the fitting profiles to draw the k2v and kr peaks from the double peaked profiles for Mg II k and C II 1334.53 Å. Finally, we have checked the correlation between Doppler velocity difference (k2r–k2v) and the FWHM of negative Gaussian for Mg II k 2976.35 Å as well as C II 1334.53 Å. The estimated correlations are shown in Figure 14. The bottom left panel shows the correlation for Mg II k 2796.35 Å (panel (c); Figure 14) while the bottom right panel shows this correlation for C II 1334.53 Å. In the case of Data set 1, we have found a very positive correlation for both lines (i.e., Mg II k) with the Pearson coefficient of 0.799. Similarly, the C II k line also shows a very good correlation between velocity difference and FWHM of negative Gaussian with the Pearson coefficient of 0.809. We have also found similar results for other data sets (i.e., Data set 2 and Data set 3), which are not shown here. Thus this analysis validates that negative Gaussian basically captures the dynamics of the dip region (for Mg II k and C II lines), which originates from the upper chromosphere (Leenaarts et al. 2013; Rathore et al. 2015). Our adopted methodology is different from that of Schmit et al. (2015) to tackle the optically thick lines. Schmit et al. (2015) have utilized the best-fitted profiles to estimate various parameters of Mg II h 2803.53 Å; however, we have used the parameters from negative Gaussian to characterize the upper

chromosphere. The motive behind the correlation (correlation between velocity difference and FWHM of negative Gaussian) is to emphasize that dynamics/activities are really captured by negative Gaussian. In addition, our adopted method also shows consistency with Schmit et al. (2015).

ORCID iDs

Yamini K. Rao https://orcid.org/0000-0002-8050-924X

References

Benz, A. O. 2008, LRSP, 5, 1
Bradshaw, S. J., & Cargill, P. J. 2005, A&A, 437, 311
Brekke, P., Hassler, D. M., & Wilhelm, K. 1997, SoPh, 175, 349
Cargill, P. J., & Bradshaw, S. J. 2013, ApJ, 772, 40
Carlsson, M., Leenaarts, J., & De Pontieu, B. 2015, ApJL, 809, L30
Chae, J., Wang, H., Qiu, J., Goode, P. R., & Wilhelm, K. 2000, ApJ, 533, 535
Chae, J., Yun, H. S., & Poland, A. I. 1998, ApJS, 114, 151
Dadashi, N., Teriaca, L., & Solanki, S. K. 2011, A&A, 534, A90
De Pontieu, B., Title, A. M., Lemen, J. R., et al. 2014, SoPh, 289, 2733
Dowdy, J. F., Jr. 1993, ApJ, 411, 406
Doyle, J. G., Taroyan, Y., Ishak, B., Madjarska, M. S., & Bradshaw, S. J. 2006, A&A, 452, 1075
Feldman, U. 1998, ApJ, 507, 974
Foukal, P. V. 1976, ApJ, 210, 575
Hansteen, V. 1993, ApJ, 402, 741
Hansteen, V., De Pontieu, B., Carlsson, M., et al. 2014, Sci, 346, 1255757
Harra, L. K., Sakao, T., Mandrini, C. H., et al. 2008, ApJL, 676, L147
Hood, A. W., & Priest, E. R. 1981, GApFD, 17, 297
Huang, Z., Xia, L., Li, B., & Madjarska, M. S. 2015, ApJ, 810, 46
Kayshap, P., Banerjee, D., & Srivastava, A. K. 2015, SoPh, 290, 2889
Kayshap, P., Tripathi, D., Solanki, S. K., & Peter, H. 2018, ApJ, 864, 21
Klimchuk, J. A. 2006, SoPh, 234, 41
Landi, E. 2007, ApJ, 663, 1363
Leenaarts, J., Pereira, T. M. D., Carlsson, M., Uitenbroek, H., & De Pontieu, B. 2013, ApJ, 772, 90
Lenz, D. D., DeLuca, E. E., Golub, L., Rosner, R., & Bookbinder, J. A. 1999, ApJL, 517, L155
Morrill, J. S., Dere, K. P., & Korendyke, C. M. 2001, ApJ, 557, 854
Patsourakos, S., & Klimchuk, J. A. 2006, ApJ, 647, 1452
Peter, H., & Judge, P. G. 1999, ApJ, 522, 1148
Polito, V., Reeves, K. K., Del Zanna, G., Golub, L., & Mason, H. E. 2015, ApJ, 803, 84
Rathore, B., Carlsson, M., Leenaarts, J., & De Pontieu, B. 2015, ApJ, 811, 81
Reale, F. 2014, LRSP, 11, 4
Rosner, R., Tucker, W. H., & Vaiana, G. S. 1978, ApJ, 220, 643
Sasso, C., Andretta, V., Spadaro, D., & Susino, R. 2012, A&A, 537, A150
Schmit, D., Bryans, P., De Pontieu, B., et al. 2015, ApJ, 811, 127
Spadaro, D., Lanza, A. F., Lanzafame, A. C., et al. 2003, ApJ, 582, 486
Stucki, K., Solanki, S. K., Schühle, U., et al. 2000, A&A, 363, 1145
Taroyan, Y., Erdélyi, R., Doyle, J. G., & Bradshaw, S. J. 2005, A&A, 438, 713
Teriaca, L., Banerjee, D., & Doyle, J. G. 1999, A&A, 349, 636
Tian, H., DeLuca, E., Reeves, K. K., et al. 2014, ApJ, 786, 137
Tian, H., Marsch, E., Curdt, W., & He, J. 2009, ApJ, 704, 883
Tian, H., Tu, C.-Y., Marsch, E., He, J.-S., & Zhou, G.-Q. 2008, A&A, 478, 915
Warren, H. P., Mariska, J. T., & Wilhelm, K. 1997, ApJL, 490, L187
Warren, H. P., Winebarger, A. R., & Hamilton, P. S. 2002, ApJL, 579, L41
Zacharias, P., Hansteen, V. H., Leenaarts, J., Carlsson, M., & Gudiksen, B. V. 2018, A&A, 614, A110